ELSEVIER

International Journal of Solids and Structures 41 (2004) 1263–1284

INTERNATIONAL JOURNAL OF SOLIDS and STRUCTURES

www.elsevier.com/locate/ijsolstr

Rate-dependent quasi-flow corner theory for elastic/visco-plastic materials

Ping Hu *

Department of Automobile Body Engineering, State Key Laboratory of Automotive Dynamic Simulation, Institute of Automobile Body and Die Engineering, Nanling Campus of Jilin University, Renmin Strees No. 142, Changchun 130025, China

Received 7 August 2003; received in revised form 3 September 2003

Abstract

A rate-dependent quasi-flow plastic constitutive model with punch-speed sensitivity is proposed for the large-deformation sheet metal forming process, which is based on the quasi-flow corner theory and *U–L* formulation for the virtual work-rate equation. Three kinds of constitutive theories with strain rate dependence, classical flow theory, deformation theory with rate form obeying non-orthogonality rule, and the present quasi-flow corner theory, are introduced into the *U–L* finite element formulation to simulate the deformation localization processes of plane strain tension in order to investigate effects of strain rate sensitivity on the localizing deformation characters. Furthermore, three kinds of typical forming processes sheet metals, one being an uniaxial stretching and another being a square cup drawing with circular blank, and third being a deep drawing of an oil pan, actual industrial forming part, are also numerically simulated by the present model and compared with experimental results. Good agreement between numerical simulation and experimental ones exhibits the validity of the quasi-flow corner theory.

Keywords: Punch-speed sensitivity; Rate-dependent quasi-flow plastic constitutive model; Plane strain tension; Sheet metal forming

1. Introduction

In most automobile manufacturing companies, stamping CAE technique is widely adopted and introduced for the purpose of predicting forming defects of stamped sheet panels and saving tool modification man-hours. Due to complicated forming process and a large number of relative influence factors for the sheet metal forming, it is important to provide more effective and more accurate CAE software. In these influence factors, in general, punch speed is one of them, which is sensitive to the formability of the stamped sheet panels and the stamping process. For example, for a deep-drawing panel with large plastic deformation, the formability obtained by hydraulic pressure and mechanical pressure is obviously different. In

* Tel.: +86-431-568-7162; fax: +86-431-570-5762.
E-mail address: pinghu@jlu.edu.cn (P. Hu).

0020-7683/$ - see front matter © 2003 Elsevier Ltd. All rights reserved.
doi:10.1016/j.ijsolstr.2003.09.013

many deep-drawing processes, the product can be easily formed by the hydraulic pressure with low punch speed, but, cannot by the mechanical pressure with high punch speed.

During the past two decades, considerable attention has been devoted to the development of commercial CAE software based on dynamic explicit finite element algorithm, such as DYNA3D, PAM-STAMP and OPTRIS. However, the algorithm is difficult to reflect effects of actual punch speed, if the initial speed field used in the explicit algorithm is much higher than the actual punch speed; on the other hand, overlong solving time is almost insufferable if the actual speed is taken as initial speed field. The effects of the actual punch speed can be actually introduced into the constitutive equations based on static implicit derived by Kim et al. (1978) or explicit finite element algorithm with strain rate-dependency proposed by McMeeking and Rice (1975).

Up to now, there have been some researches of the rate-dependent numerical analysis on sheet metal forming, in which the effect of strain rate is an important parameter for forming processes. Among these researches, two typical formulation methods were widely used. Park et al. (1987) and Germain and his coworkers (1989) proposed their rigid-viscoplastic finite element methods, respectively; Chandra (1986) developed a generalized elastic-viscoplastic FEM; Hart (1976) researched the constitutive relations of nonelastic deformation of metals; Huang and Liu (1994) presented the elastic-viscoplastic finite element model based on an updated Lagrangian formulation and a small increment method; Needlemen and coworkers (1988, 1989) studied material rate-dependence and mesh sensitivity in the localization deformation for simple shearing and planar uniform tension processes. Above methods were, in fact, limited to only analyze 2-D sheet metal forming process.

It should be mentioned that up to now, all of the methods or algorithms whether explicit or static implicit finite element formulation have been based on classical plastic constitutive law obeying orthogonality rule. However, the deep-drawing process of sheet metal panel with large plastic deformation observes strong nonlinear characteristics and involves complicated loading and unloading histories even strain localization phenomenon, such as local necking, wrinkling and fracturing. It is well known that the complicated deformation histories and strain localization are sensitive to the constitutive law used in the sheet metal forming simulation. It has also been noted that on the strain localization analysis for some simple tests, such as the uniaxial tension, the finite element methods using the classical plastic constitutive theory based on orthogonality rule often obtain disagreement results compared with experiments. Therefore, around this subject of strain localization for elastic–plastic solids, many researchers proposed a group of plastic constitutive theories based on non-orthogonality rule. Budiansky (1959), Storen and Rice (1975) and Hutchinson (1974) developed a vertex hardening constitutive model based on the rate form of the J_2 deformation theory, which provides more accurate predictions for the buckling process of sheet metal than the classical flow theory of plasticity does. Christofferson and Hutchinson (1979) proposed a class of plastic constitutive equations with vertex effect in which the plastic potential is introduced as a function of stress increment, and a smooth transition from plastic loading to elastic unloading is incorporated. Its simplest form called J_2 corner theory was then applied to several localization problems. Based on tensor algebra, Gotoh (1985) proposed a group of plastic constitutive equations in which the vertex effect satisfies mathematical restriction about tensor functions. Neale (1981) gave excellent review to these constitutive equations in his summarizing paper. It should be also noted that according to the experimental work for the polycrystalline material, the original yield surface has a corner due to the slip deformation of crystal. Therefore, the so-called corner theories above are consistent with the experimentally observed evidence.

A common feature of these constitutive theories is that the non-orthogonality rule between plastic strain increment and yield surface is observed throughout the whole plastic deformation process from initial yielding up to final strain localization and fracture. From the point of view of plastic potential and classical flow theory, it is generally acknowledged that in the initial stage of plastic deformation, the yield surface should be convex and smooth and consistent with the normality rule of plastic flow. However, strain localization of sheet metal forming always occurs at the final stage of plastic deformation where the suc-

ceeding "yield surface" will gradually appear as a vertex effect. According to the above discussions, Hu et al. (1998a,b) proposed a quasi-flow corner constitutive law with no rate-dependency. In this paper, the rate-dependent quasi-flow corner plastic theory with punch speed sensitivity is proposed on the basis of the quasi-flow corner constitutive law and the static explicit *U–L* formulation for the virtual power equation proposed by Hu et al. (1998, 2001, 2002), and then three kinds of plasticity constitutive theories with strain rate dependence, J2F, J2D derived by Budiansky (1959), and by Storen and Rice (1975) and the present quasi-flow corner theory, are used to simulate the strain localization deformation processes of plane strain tension problem. Besides, the numerical simulation of an uniaxial stretching, a square cup drawing with circular blank, and a deep drawing process of an oil pan is carried out as well. The focus of the present research is to investigate effects of strain rate sensitivity exponent and tension speed for the plane strain tension (punch speed for sheet metal stamping) on the localizing deformation characters such as tensile strengthening, strain localizing, necking elongation and thickness thinning of specimens. Simulated results of the three kinds of constitutive theories with rate dependence are compared and discussed in detail for the plane strain tension. And then for the sheet metal forming, validation of the simulations is performed through usage of a comparison with the experimental results of the uniaxial stretching of a HPC35 high tensional steel sheet, of the square cup drawing of a commonly used 08Al sheet, and of the deep drawing of 08ZF sheet from different punch speeds. On the final example, the deep-drawing process of an oil pan is simulated by the present QFCT model and also compared with experimental ones which further shows the validity of the present theory on simulating complicated industrial forming.

2. Analytical background

2.1. Theoretical foundations

In the past work, a new type of elastic–plastic constitutive theory, so-called quasi-flow corner theory derived by Hu et al. (1998a,b) was proposed with no rate-dependency, and some detailed discussions on different plastic constitutive equations based on non-normality rule and on isotropic *Mises* yield criterion were presented. In the QFCT, the plastic strain rate $\dot{\varepsilon}_{ij}^{\mathrm{p}}$ can be expressed as

$$\dot{\varepsilon}_{ij}^{\mathrm{p}} = \frac{3}{2}\left(\frac{1}{E_{\mathrm{Q}}} - \frac{1}{E}\right) I_{ijkl}\dot{\sigma}_{kl} + \left(\frac{3}{2\bar{\sigma}}\right)^2 \left(\frac{1}{E_{\mathrm{t}}} - \frac{1}{E_{\mathrm{Q}}}\right) \dot{J}_2 \dot{\sigma}'_{ij} \tag{1}$$

in which E_{t} is the tangent slope of the stress–strain curve under uniaxial tension,

$$E_{\mathrm{Q}} = E \times \frac{1 - 2\mu_{\mathrm{Q}}}{1 - 2\mu}, \tag{2}$$

$$\mu_{\mathrm{Q}} = 0.5 - g(\bar{\varepsilon}_{\mathrm{p}})(0.5 - \mu), \tag{3}$$

$$I_{ijkl} = \frac{1}{2}(\delta_{ik}\delta_{jl} + \delta_{il}\delta_{jk}) - \frac{1}{3}\delta_{ij}\delta_{kl}, \tag{4}$$

where E and μ are the common Young's modulus and Poisson ratio, respectively, and $g(\bar{\varepsilon}_{\mathrm{p}})$ is a modulus evolutional function with respect to the current effective plastic strain $\bar{\varepsilon}_{\mathrm{p}}$, which can be generally written as

$$g(\bar{\varepsilon}_{\mathrm{p}}) = \frac{1}{2}\left(1 + \frac{E_{\mathrm{S}}}{E}\right) - \frac{1}{\pi}\left(1 - \frac{E_{\mathrm{S}}}{E}\right) \mathrm{tg}^{-1}\left(\frac{\bar{\varepsilon}_{\mathrm{p}} - \bar{\varepsilon}_{\mathrm{p}}^{0}}{a_0}\right), \tag{5}$$

where E_{S} is the secant modulus of the stress–strain curve under uniaxial tension, a_0 is a small constant related to the strain hardening exponent n, and $\bar{\varepsilon}_{\mathrm{p}}^{0}$ is a transitional threshold strain value where E_{Q}

transforms to E_S, and is related to material characters and plastic deformation manners. According to the model proposed by Hu et al. (1998a,b, 2001), in no less of generality, the $\bar{\varepsilon}_p^0$ and a_0 values are taken to be n and $0.04n$, respectively. Now, we assume that

$$\frac{1}{H_Q} = \left(\frac{1}{E_Q} - \frac{1}{E}\right), \qquad \frac{1}{H} = \left(\frac{1}{E_t} - \frac{1}{E}\right) \tag{6}$$

if noting that

$$I_{ijkl}\dot{\sigma}_{kl} = \dot{\sigma}'_{ij} \tag{7}$$

and

$$H = \frac{\dot{\bar{\sigma}}}{\dot{\bar{\varepsilon}}_p} \tag{8}$$

where $\dot{\bar{\sigma}}$ and $\dot{\bar{\varepsilon}}^p$ are effective stress rate and effective plastic strain rate, respectively, the following equation can be obtained:

$$\dot{\varepsilon}^p_{ij} = \dot{\bar{\varepsilon}}_p p_{ij} + \frac{3}{2H_Q}\dot{\sigma}'_{ij} - p_{ij}\frac{\dot{\bar{\sigma}}}{H_Q} \tag{9}$$

in which

$$p_{ij} = 3\sigma'_{ij}/(2\bar{\sigma}). \tag{10}$$

The total strain rate $\dot{\varepsilon}_{ij}$ can be expressed as

$$\dot{\varepsilon}_{ij} = \dot{\varepsilon}^e_{ij} + \dot{\varepsilon}^p_{ij} = B^e_{ijkl}\dot{\sigma}_{kl} + p_{ij}\left(\dot{\bar{\varepsilon}}_p - \frac{\dot{\bar{\sigma}}}{H_Q}\right) + \frac{3}{2H_Q}\dot{\sigma}'_{ij}, \tag{11}$$

where

$$B^e_{ijkl} = D^{e^{-1}}_{ijkl} \tag{12}$$

and

$$D^e_{ijkl} = \frac{E}{1+\mu}\left[\delta_{ik}\delta_{jl} + \frac{\mu}{1-2\mu}\delta_{ij}\delta_{kl}\right]. \tag{13}$$

Considering that $\delta_{kl}\sigma'_{kl} = 0$, $\delta_{kl}\dot{\sigma}'_{kl} = 0$, $G = \frac{E}{2(1+\mu)}$ and $D^e_{ijkl}\sigma'_{kl} = \frac{E}{1+\mu}\sigma'_{ij} = 2G\sigma'_{ij}$, Eq. (11) becomes

$$\dot{\sigma}_{ij} = D^e_{ijkl}\dot{\varepsilon}_{kl} - \frac{3G}{2H_Q}\left(\dot{\sigma}'_{ij} - \frac{\dot{\bar{\sigma}}}{\bar{\sigma}}\sigma'_{ij}\right) - \frac{3G\dot{\bar{\varepsilon}}_p}{\bar{\sigma}}\sigma'_{ij}. \tag{14}$$

In order to get an explicit expression of the constitutive equation for the QFCT with strain rate-dependency, it is necessary to express $\dot{\bar{\sigma}}$ and σ'_{ij} in Eq. (14) by using strain rate. Considering that

$$\dot{\bar{\sigma}} = \frac{3}{2\bar{\sigma}}\sigma'_{kl}\dot{\sigma}_{kl} \tag{15}$$

we have

$$\dot{\bar{\sigma}} = \frac{3}{2\bar{\sigma}}\sigma'_{ij}\left[D^e_{ijkl}\dot{\varepsilon}_{kl} - \frac{3G\dot{\bar{\varepsilon}}_p}{\bar{\sigma}}\sigma'_{ij} - \frac{3G}{H_Q}\left(\dot{\sigma}'_{ij} - \frac{\dot{\bar{\sigma}}}{\bar{\sigma}}\sigma'_{ij}\right)\right]. \tag{16}$$

Noting that $\sigma'_{ij}\sigma'_{ij} = \frac{2}{3}\bar{\sigma}^2$, $\dot{\sigma}'_{ij} = \dot{\sigma}_{ij} - \frac{1}{3}\delta_{ij}\dot{\sigma}_{kk}$ and $\dot{\sigma}_{kk} = \frac{E}{1-2\mu}\dot{\varepsilon}_{kk}$, $\dot{\bar{\sigma}}$ and σ'_{ij} can be written as

$$\begin{cases} \dot{\bar{\sigma}} = \frac{3G}{\bar{\sigma}}(\sigma'_{ij}\dot{\varepsilon}_{ij} - \bar{\sigma}\dot{\bar{\varepsilon}}_{\mathrm{p}}), \\ \dot{\sigma}'_{ij} = \dot{\sigma}_{ij} - \frac{1}{3}\delta_{ij}\frac{2G(1+\mu)}{1-2\mu}\dot{\varepsilon}_{kk}. \end{cases} \tag{17}$$

Introducing Eq. (17) into Eq. (14), we have

$$\dot{\sigma}_{ij} = D^{\mathrm{e}}_{ijkl}\dot{\varepsilon}_{kl} - \frac{3G}{H_{\mathrm{Q}}}\dot{\sigma}'_{ij} + \frac{3G}{H_{\mathrm{Q}}}\left\{\frac{1}{3}\delta_{ij}\delta_{kl}\dot{\varepsilon}_{kl}\frac{2G(1+\mu)}{1-2\mu} + \frac{3G}{\bar{\sigma}^2}\sigma'_{ij}\sigma'_{kl}\dot{\varepsilon}'_{kl} - \frac{3G}{\bar{\sigma}}\dot{\bar{\varepsilon}}_{\mathrm{p}}\sigma'_{ij}\right\} - \frac{3G}{\bar{\sigma}}\dot{\bar{\varepsilon}}_{\mathrm{p}}\sigma'_{ij}. \tag{18}$$

Finally, the constitutive equation of QFCT with strain rate-dependency is obtained as follows:

$$\dot{\sigma}_{ij} = \frac{H_{\mathrm{Q}}}{H_{\mathrm{Q}} + 3G}\left\{D^{\mathrm{e}}_{ijkl} + \frac{3G}{H_{\mathrm{Q}}}\left[\frac{1}{3}\delta_{ij}\delta_{kl}\frac{E}{1-2\mu} + \frac{3G}{\bar{\sigma}^2}\sigma'_{ij}\sigma'_{kl}\right]\right\}\dot{\varepsilon}_{kl} - \frac{3G}{\bar{\sigma}}\sigma'_{ij}\dot{\bar{\varepsilon}}_{\mathrm{p}}. \tag{19}$$

Assuming that

$$L_{ijkl} = \frac{H_{\mathrm{Q}}}{H_{\mathrm{Q}} + 3G}\left\{D^{\mathrm{e}}_{ijkl} + \frac{3G}{H_{\mathrm{Q}}}\left[\frac{1}{3}\frac{E}{1-2\mu}\delta_{ij}\delta_{kl} + \frac{3G}{\bar{\sigma}^2}\sigma'_{ij}\sigma'_{kl}\right]\right\} \tag{20}$$

and

$$p_{ij} = \frac{3}{2\bar{\sigma}}\sigma'_{ij}, \tag{21}$$

it can be easily proved that

$$P_{ij} = \frac{3G}{\bar{\sigma}}\sigma'_{ij} = L_{ijkl}p_{kl} \tag{22}$$

and

$$p_{ij}P_{ij} = \frac{3}{2\bar{\sigma}}\sigma'_{ij}\frac{3G}{\bar{\sigma}}\sigma'_{ij} = 3G. \tag{23}$$

So, the constitutive equation of QFCT with strain rate-dependency is obtained by

$$\dot{\sigma}_{ij} = L_{ijkl}\dot{\varepsilon}_{kl} - \dot{\bar{\varepsilon}}_{\mathrm{p}}P_{ij}. \tag{24}$$

In addition, the effective stress rate $\dot{\bar{\sigma}}$ can be written as

$$\dot{\bar{\sigma}} = P_{ij}\dot{\varepsilon}_{ij} - \dot{\bar{\varepsilon}}_{\mathrm{p}}p_{ij}P_{ij}. \tag{25}$$

It should be noted from Eqs. (6) and (24) that H_{Q} becomes infinite when E_{Q} trends to E, and moreover, L_{ijkl} in Eq. (20) will fall back on D^{e}_{ijkl}.

Now, one introduces the general yield criterion under uniaxial stress state and relating to strain rate sensitivity as follows:

$$\phi(\bar{\sigma}, \bar{\varepsilon}_{\mathrm{p}}, \dot{\bar{\varepsilon}}_{\mathrm{p}}) = 0 \tag{26}$$

or

$$\dot{\bar{\varepsilon}}_{\mathrm{p}} = \Psi(\bar{\sigma}, \bar{\varepsilon}_{\mathrm{p}}), \tag{27}$$

where $\bar{\sigma}$, $\bar{\varepsilon}_{\mathrm{p}}$ and $\dot{\bar{\varepsilon}}_{\mathrm{p}}$ are *Cauchy* effective stress, effective plastic strain and effective plastic strain rate, respectively. In no less of generality, the common *Holloman* formula $\bar{\sigma} = A(\bar{\varepsilon}_{\mathrm{p}} + \bar{\varepsilon}^0_{\mathrm{p}})^n(\frac{\dot{\bar{\varepsilon}}_{\mathrm{p}}}{\dot{\bar{\varepsilon}}^0_{\mathrm{p}}})^m$ is used, in which $\bar{\varepsilon}^0_{\mathrm{p}}$, $\dot{\bar{\varepsilon}}^0_{\mathrm{p}}$, n and m are initial plastic strain, initial plastic-strain rate, strain hardening exponent and strain rate sensitivity exponent, respectively. So, Eq. (27) can be written as

$$\dot{\bar{\varepsilon}}_{\mathrm{p}} = \Psi(\bar{\sigma}, \bar{\varepsilon}_{\mathrm{p}}) = \left(\frac{\bar{\sigma}}{A(\bar{\varepsilon}_{\mathrm{p}} + \bar{\varepsilon}_{\mathrm{p}}^0)^n} \right)^{\frac{1}{m}} \cdot \dot{\bar{\varepsilon}}_{\mathrm{p}}^0. \tag{28}$$

As a result, one has

$$\frac{\partial \dot{\bar{\varepsilon}}_{\mathrm{p}}}{\partial \bar{\sigma}} = \frac{\dot{\bar{\varepsilon}}_{\mathrm{p}}^0}{m} \left(\frac{\bar{\sigma}}{A(\bar{\varepsilon}_{\mathrm{p}} + \bar{\varepsilon}_{\mathrm{p}}^0)^n} \right)^{\frac{1}{m}-1} \frac{1}{A(\bar{\varepsilon}_{\mathrm{p}} + \bar{\varepsilon}_{\mathrm{p}}^0)^n} \tag{29}$$

and

$$\frac{\partial \dot{\bar{\varepsilon}}_{\mathrm{p}}}{\partial \bar{\varepsilon}_{\mathrm{p}}} = \frac{\bar{\sigma}\dot{\bar{\varepsilon}}_{\mathrm{p}}^0}{Am} \left(\frac{\bar{\sigma}}{A(\bar{\varepsilon}_{\mathrm{p}} + \bar{\varepsilon}_{\mathrm{p}}^0)^n} \right)^{\frac{1}{m}-1} \left(- \frac{n}{(\bar{\varepsilon}_{\mathrm{p}} + \bar{\varepsilon}_{\mathrm{p}}^0)^{n+1}} \right). \tag{30}$$

2.2. Introduction of punch-speed dependence

Effect of the punch-speed $\dot{u}$ on sheet metal formability in industrial stamping processes can be introduced by the above strain rate-dependent quasi-flow corner theory and the *Hollomon* formula. In no less of generality, the punch-speed $\dot{u}$ can be expressed as

$$\dot{u} = \frac{\Delta\omega}{\Delta t}, \tag{31}$$

where $\Delta\omega$ and Δt mean the displacement increment of moving punch and the time increment corresponding to $\Delta\omega$, respectively. In general, punch speed is a known parameter imported by users, and can be considered as a constant. Even now, the punch speed values of mechanical press and hydraulic pressure are different. Provided that the punch speed is a variable, the curve of the speed in terms of punch journey should be given. In the numerical simulation of sheet metal forming process, all of the mechanical variables at the time t are assumed to be known. Once the speed $\dot{u}$ is given, the speed sensitivity character can be introduced into above constitutive equation by the following tangent-coefficient scheme, due to very small time increment step Δt.

Now, one defines the effective plastic strain increment $\Delta\bar{\varepsilon}_{\mathrm{p}}$ from time t to $t + \Delta t$ by

$$\Delta\bar{\varepsilon}_{\mathrm{p}} = \bar{\varepsilon}_{\mathrm{p}}(t + \Delta t) - \bar{\varepsilon}_{\mathrm{p}}(t). \tag{32}$$

Within the time interval from t to $t + \Delta t$, the displacement increment $\Delta\omega$ of the moving punch is previously determined by the total displacement difference between time t and $t - \Delta t$. For the given speed $\dot{u}$, the time increment step Δt is obtained by Eq. (31) and used for all of material elements. Further, the above equation can be linearly interpolated in term of Δt and approximately expressed as

$$\Delta\bar{\varepsilon}_{\rho} = \Delta t \left\{ (1 - \theta)\dot{\bar{\varepsilon}}_{\rho}(t) + \theta\dot{\bar{\varepsilon}}_{\rho}(t + \Delta t) \right\} \tag{33}$$

in which $0 \leqslant \theta \leqslant 1$. It can be obviously found that when $\theta = 0$, 0.5 and 1.0, Eq. (32) is just about the formulation formula of Euler method, *Crank–Niokolson* method and full implicit time integrating method, respectively. On the other hand, the plastic strain rate at $t + \Delta t$ can be approximately expressed as

$$\dot{\bar{\varepsilon}}_{\rho}(t + \Delta t) = \dot{\bar{\varepsilon}}_{\rho}(t) + \frac{\partial \dot{\bar{\varepsilon}}_{\rho}}{\partial \bar{\sigma}} \Delta\bar{\sigma} + \frac{\partial \dot{\bar{\varepsilon}}_{\rho}}{\partial \bar{\varepsilon}_{\rho}} \Delta\bar{\varepsilon}_{\rho}. \tag{34}$$

Introducing Eq. (33) into the above equation, one has

$$\dot{\bar{\varepsilon}}_\rho(t+\Delta t) = \dot{\bar{\varepsilon}}_\rho(t) + (\Delta t)^2\theta\left\{\frac{\partial\dot{\bar{\varepsilon}}_\rho}{\partial\bar{\sigma}}\ddot{\bar{\sigma}} + \frac{\partial\dot{\bar{\varepsilon}}_\rho}{\partial\bar{\varepsilon}_\rho}\dot{\bar{\varepsilon}}_\rho\right\} \tag{35}$$

in which $\ddot{\bar{\sigma}} = \frac{\Delta\dot{\bar{\sigma}}}{\Delta t}$ and $\dot{\bar{\varepsilon}}_\rho = \frac{\Delta\bar{\varepsilon}_\rho}{\Delta t}$. It must be mentioned that the meaning of $\Delta\bar{\varepsilon}_\rho$ in Eq. (34) is different with that in Eq. (33), that is to say, $\dot{\bar{\varepsilon}}_\rho \neq \dot{\bar{\varepsilon}}_\rho(t)$. In order to distinguish them, the $\Delta\bar{\varepsilon}_\rho$ value in Eq. (34) is marked as $\Delta\tilde{\varepsilon}_\rho$.

In addition, in terms of *Mises* yield criterion, the *Cauchy* effective stress rate $\dot{\bar{\sigma}}$ can be expressed as $\dot{\bar{\sigma}} = \frac{3}{2\bar{\sigma}}\sigma'_{ij}\dot{\sigma}_{ij} = p_{ij}\dot{\sigma}_{ij}$. Therefore, in terms of Eq. (24), the *Cauchy* effective stress increment $\Delta\bar{\sigma}$ can also be written as

$$\Delta\bar{\sigma} = \Delta t\dot{\bar{\sigma}} = \Delta t(p_{ij}L_{ijkl}\dot{\varepsilon}_{kl} - p_{ij}P_{ij}\dot{\bar{\varepsilon}}_{\mathrm{p}}) = \Delta tP_{ij}\dot{\varepsilon}_{ij} - \Delta\tilde{\varepsilon}_{\mathrm{p}}P_{ij}p_{ij}. \tag{36}$$

From Eq. (24), (34)–(36), one has

$$\Delta\tilde{\varepsilon}_{\mathrm{p}} = \Delta t\dot{\bar{\varepsilon}}_{\mathrm{p}}(t) + (\Delta t)^2\theta P_{ij}\dot{\varepsilon}_{ij}\frac{\partial\dot{\bar{\varepsilon}}_{\mathrm{p}}}{\partial\bar{\sigma}} + \Delta t\theta\Delta\tilde{\varepsilon}_{\mathrm{p}}\left(\frac{\partial\dot{\bar{\varepsilon}}_{\mathrm{p}}}{\partial\bar{\varepsilon}_{\mathrm{p}}} - \frac{\partial\dot{\bar{\varepsilon}}_{\mathrm{p}}}{\partial\bar{\sigma}}p_{ij}P_{ij}\right). \tag{37}$$

The above equation can be further written as

$$\Delta\tilde{\varepsilon}_{\mathrm{p}}\left[1 + \Delta t\theta\frac{\partial\dot{\bar{\varepsilon}}_{\mathrm{p}}}{\partial\bar{\sigma}}\left(p_{ij}P_{ij} - \frac{\partial\dot{\bar{\varepsilon}}_{\mathrm{p}}}{\partial\bar{\varepsilon}_{\mathrm{p}}}\frac{\partial\bar{\sigma}}{\partial\dot{\bar{\varepsilon}}_{\mathrm{p}}}\right)\right] = \Delta t\dot{\bar{\varepsilon}}_{\mathrm{p}}(t) + (\Delta t)^2\theta P_{ij}\dot{\varepsilon}_{ij}\frac{\partial\dot{\bar{\varepsilon}}_{\mathrm{p}}}{\partial\bar{\sigma}}. \tag{38}$$

Assuming that

$$\xi = \Delta t\cdot\theta\frac{\partial\dot{\bar{\varepsilon}}_{\mathrm{p}}}{\partial\bar{\sigma}}\cdot h, \tag{39}$$

in which

$$h = p_{ij}P_{ij} - \frac{\partial\dot{\bar{\varepsilon}}_{\mathrm{p}}}{\partial\bar{\varepsilon}_{\mathrm{p}}}\frac{\partial\bar{\sigma}}{\partial\dot{\bar{\varepsilon}}_{\mathrm{p}}} = p_{ij}L_{ijkl}p_{kl} - \frac{\partial\dot{\bar{\varepsilon}}_{\mathrm{p}}}{\partial\bar{\varepsilon}_{\mathrm{p}}}\frac{\partial\bar{\sigma}}{\partial\dot{\bar{\varepsilon}}_{\mathrm{p}}}, \tag{40}$$

one can obtain

$$\Delta\tilde{\varepsilon}_{\mathrm{p}}(1+\xi) = \Delta t\dot{\bar{\varepsilon}}_{\mathrm{p}}(t) + (\Delta t)^2\theta P_{ij}\dot{\varepsilon}_{ij}\frac{\partial\dot{\bar{\varepsilon}}_{\mathrm{p}}}{\partial\bar{\sigma}}. \tag{41}$$

Noting that

$$\frac{1}{h}\frac{\xi}{1+\xi} = \frac{1}{h}\frac{\Delta t\cdot\theta\frac{\partial\dot{\bar{\varepsilon}}_{\mathrm{p}}}{\partial\bar{\sigma}}\cdot h}{1+\xi} = \frac{\Delta t\theta}{1+\xi}\frac{\partial\dot{\bar{\varepsilon}}_\rho}{\partial\bar{\sigma}} \tag{42}$$

one has

$$\Delta\tilde{\varepsilon}_{\mathrm{p}} = \Delta t\left\{\frac{\dot{\bar{\varepsilon}}_\rho(t)}{1+\xi} + \frac{1}{h}\frac{\xi}{1+\xi}\cdot P_{ij}\dot{\varepsilon}_{ij}\right\} \tag{43}$$

and

$$\dot{\bar{\varepsilon}}_{\mathrm{p}} = \frac{\dot{\bar{\varepsilon}}_{\mathrm{p}}(t)}{1+\xi} + \frac{1}{h}\frac{\xi}{1+\xi}\cdot P_{ij}\dot{\varepsilon}_{ij}. \tag{44}$$

Obviously, if taking $\theta = 0$, one has $\xi = 0$. It can be easily found from the above equation that

$$\dot{\bar{\varepsilon}}_{\mathrm{p}} = \dot{\bar{\varepsilon}}_{\mathrm{p}}(t). \tag{45}$$

Introducing Eq. (44) into Eq. (24), the constitutive equation of QFCT with strain rate-dependency is rewritten as follows:

$$\dot{\sigma}_{ij} = \hat{L}_{ijkl}\dot{\varepsilon}_{kl} - \frac{\dot{\bar{\varepsilon}}_{\mathrm{p}}(t)}{1+\xi}P_{ij} \tag{46}$$

in which

$$\hat{L}_{ijkl} = L_{ijkl} - \frac{1}{h}\frac{\xi}{1+\xi}P_{ij}P_{kl}. \tag{47}$$

For a given $\dot{u}$ value in Eq. (31), using Eqs. (39) and (47), the effect of punch-speed sensitivity on constitutive model can be introduced.

3. Finite element formulation

In finite elasto-plasticity, the basic kinematic assumption is the multiplicative decomposition of total deformation gradient. The total strain description in small strain range must be coincided with the finite strain formulation of elastic–plastic solids. Considering that most of sheet metal in plastic forming are of infinite elasticity and finite plasticity, a simple remedy is to replace the strain rate $\dot{\varepsilon}_{ij}$ and $\dot{\sigma}_{ij}$ in Eq. (46) by the deformation rate $\dot{d}_{ij}$ and the *Jaumann* rate $\overset{\nabla}{\sigma}_{ij}$ of *Cauchy* stress defined relative to current material configuration, respectively. In this case, Eq. (46) is written as

$$\overset{\nabla}{\sigma}_{ij} = \hat{L}_{ijkl}\dot{d}_{kl} - P_{ij}\frac{\dot{\bar{\varepsilon}}_{\mathrm{p}}(t)}{1+\xi}. \tag{48}$$

Now, the virtual power equation described by the updated *Lagrangian* form is used to the present finite element formulation, which can be generally written as

$$\int_{V^{\mathrm{e}}} \dot{t}_{ij}\,\delta\dot{l}_{ji}\,\mathrm{d}V = \int_{V^{\mathrm{e}}} \dot{g}_i\,\delta\dot{v}_i\,\mathrm{d}V + \int_{A_\sigma} \dot{\bar{g}}_i\,\delta\dot{v}_i\,\mathrm{d}S, \tag{49}$$

where $\dot{t}_{ij}$ is the first *Poila–Kirchhoff* stress rate tensor, and $\dot{l}_{ji}$ is velocity gradient. Considering the incompressibility condition of plastic deformation volume, $\dot{t}_{ij}$ is related to the *Jaumann* rate $\overset{\nabla}{\sigma}_{ij}$ of the *Cauchy* stress σ_{ij} by

$$\dot{t}_{ij} = \overset{\nabla}{\sigma}_{ij} - \sigma_{ik}\dot{d}_{kj} - \sigma_{jk}\dot{d}_{ki} + \sigma_{ik}v_{j,k}. \tag{50}$$

Introducing Eqs. (48) and (50) into Eq. (49), and considering the symmetry of the tensor P_{ij} in Eq. (21) and further the *Jaumann* rate $\overset{\nabla}{\sigma}_{ij}$, one obtains

$$\begin{aligned}&\int_{V^{\mathrm{e}}} \hat{L}_{ijkl}\dot{d}_{kl}\,\delta\dot{d}_{ij}\,\mathrm{d}V + \int_{V^{\mathrm{e}}} (\sigma_{ik}v_{j,k} - \sigma_{ki}\dot{d}_{kj} - \sigma_{kj}\dot{d}_{ki})\,\delta\dot{l}_{ji}\,\mathrm{d}V \\ &\quad = \int_{V^{\mathrm{e}}} \dot{g}_i\,\delta\dot{v}_i\,\mathrm{d}V + \int_{V^{\mathrm{e}}} P_{ij}\frac{\dot{\bar{\varepsilon}}^{\mathrm{p}}(t)}{1+\xi}\,\delta\dot{d}_{ij}\,\mathrm{d}V + \int_{A_\sigma} \dot{\bar{g}}_i\,\delta\dot{v}_i\,\mathrm{d}V.\end{aligned} \tag{51}$$

One defines that

$$Q_{ijkl} = \sigma_{lj}\delta_{ki} \tag{52}$$

and

$$F_{ijkl} = \frac{1}{2}(\sigma_{kj}\delta_{li} + \sigma_{lj}\delta_{ki} + \sigma_{ki}\delta_{lj} + \sigma_{li}\delta_{kj}). \tag{53}$$

And then, one further assumes that

$$\dot{\mathbf{d}} = \mathbf{B}\dot{\mathbf{q}} \quad \text{and} \quad \dot{\mathbf{l}} = \mathbf{B}_{\mathrm{v}}\dot{\mathbf{q}} \tag{54}$$

where $\mathbf{B}$ and $\mathbf{B}_{\mathrm{v}}$ are the strain matrices corresponding to the deformation rate vector $\dot{\mathbf{d}}$ and the velocity gradient vector $\dot{\mathbf{l}}$, and $\dot{\mathbf{q}}$ is nodal velocity vector of elements. Introducing Eqs. (52)–(54) into Eq. (51), and considering the randomicity of the virtual velocity $\delta\dot{v}_i$, the discrete element stiffness equation can be generally written by using matrix form

$$\mathbf{k}\dot{\mathbf{q}} = \dot{\mathbf{p}} + \dot{\mathbf{f}} + \dot{\bar{\mathbf{f}}}, \tag{55}$$

where

$$\mathbf{k} = \int_{V^{\mathrm{e}}} \mathbf{B}^{\mathrm{T}}(\hat{\mathbf{L}} - \mathbf{F})\mathbf{B}\,\mathrm{d}V + \int_{V^{\mathrm{e}}} \mathbf{B}_{\mathrm{v}}^{\mathrm{T}}\mathbf{Q}\mathbf{B}_{\mathrm{v}}\,\mathrm{d}V, \tag{56}$$

$$\dot{\mathbf{p}} = \int_{V^{\mathrm{e}}} \mathbf{B}^{\mathrm{T}}\mathbf{P}\frac{\dot{\bar{\varepsilon}}^{\mathrm{p}}(t)}{1+\xi}\mathrm{d}V = \int_{V^{\mathrm{e}}} \mathbf{B}^{\mathrm{T}}\boldsymbol{\sigma}'\frac{3G\dot{\bar{\varepsilon}}^{\mathrm{p}}(t)}{(1+\xi)\bar{\sigma}}\mathrm{d}V, \tag{57}$$

$$\dot{\mathbf{f}} = \int_{V^{\mathrm{e}}} \mathbf{N}^{\mathrm{T}}\dot{\mathbf{g}}\,\mathrm{d}V, \tag{58}$$

$$\dot{\bar{\mathbf{f}}} = \int_{A_\sigma} \mathbf{N}^{\mathrm{T}}\dot{\bar{\mathbf{g}}}\,\mathrm{d}A. \tag{59}$$

In order to effectively simulate the strain localization and the shear bend elongation processes of the plane strain tension, and investigate the validity of the present QFCT model in simulating the post-instability problem, a so-called crossed triangles element model proposed by Nagtegaal et al. (1974) is introduced into the above *U–L* formulation. Moreover, in the sheet metal forming, a lot of experimental results with punch speed sensitivity can become more convincing comparison and examination yardsticks for the present model. Therefore, by mixing plate bending with shear strains and membrane drawing effects for large strain elastic–plastic deformation problem, a refined discrete thick/thin four-nodal quadrilateral *Mindlin* plate element (shown in Fig. 1), named as RDKQM given by Chen and Cheung (2000) based on *Mindlin/Reissner* plate theory is introduced into the present finite element formulation with rate-dependent

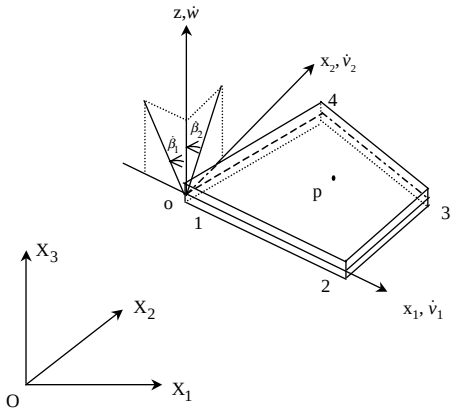

Fig. 1. Geometric description of the RDKQM element.

quasi-flow plastic constitutive model. It should be mentioned that in all of the following simulation examples, the *Crank–Niokolson* method described in Section 2.2 is used for time integration of constitutive equation (46) by taking $\theta = 0.5$ in Eq. (33).

It should be mentioned that the time integration of the constitutive equations (47) and (48) is carried out by taking widely used *Euler* method. The integrative scheme is to keep jarless change of the constitutive tensor $\hat{L}_{ijkl}$ and the modified term $P_{ij}\frac{\dot{\bar{\varepsilon}}_{\mathrm{p}}(t)}{1+\bar{\xi}}$ of stress rate in Eq. (48). According to Nagtegaal and Jong's scheme (1981), the time increment Δt in Eq. (31) should satisfy the following restricting equation:

$$(\sigma'_{ij}(t) + \overset{\nabla}{\sigma}{}'_{ij}\Delta t)(\sigma'_{ij}(t) + \overset{\nabla}{\sigma}{}'_{ij}\Delta t) = \frac{2}{3}[(1+\lambda)\bar{\sigma}_{\mathrm{S}}]^2, \tag{60}$$

where $\lambda \leqslant 1$. Once the crosshead speed $\dot{u}$ and the time increment Δt are determined, the crosshead displacement increment Δw becomes known. At the present simulation, the λ value is taken as 0.5.

4. Numerical results and discussions

4.1. Plane strain tension

To examine the validity of the present QFC theory, a finite element solution for plane strain tension test with an initial surface imperfection f_0 shown in Hu et al. (1998a,b) is presented. Based on finite strain version, three kinds of plasticity constitutive theories with strain rate-dependence, the J2-flow theory (J2F), the J2-deformation theory with rate form (J2D), and the QFC theory, are introduced into the numerical simulation tests in order to make a detailed comparison within these theories on bifurcation and post-bifurcation behaviors including strain localization and shear band formation, influence of meshing size, rate sensitivity exponent m and non-dim tensile speed v_{F}, where $v_{\mathrm{F}} = \dot{u}/(L\dot{\bar{\varepsilon}}^0_{\mathrm{p}})$. Two undeformed configurations of a quarter specimen are specified by initial length L and width W $(= L/3)$ as shown in the first one of Fig. 2(a) and (b), which are divided into 10×25 and 8×20 meshes, respectively. Material and geometrical parameters of the test are taken as follows:

$$n = 0.0625, \quad \dot{\bar{\varepsilon}}^0_{\mathrm{p}} = 10^{-3}\ 1/\mathrm{s}, \quad A = 590\ \mathrm{MPa}, \quad E = 200\ \mathrm{GPa}, \quad \mu = 0.33, \quad \text{yield strain } \bar{\varepsilon}_{\mathrm{Y}} = 0.002,$$

$$\text{yield stress } \bar{\sigma}_{\mathrm{Y}} = 400\ \mathrm{MPa}, \quad \text{initial imperfection parameter } f_0 = 0.005, \quad v_{\mathrm{F}} = 1000.$$

First, taking the rate sensitivity exponent $m = 0.001$ in Eq. (28), Fig. 2(a) and (b) show the final deformed configurations (elongation ratio $U/L = 0.14$) for localization necking and shear bands which are obtained by the three theories with non-dim tensile speed $v_{\mathrm{F}} = 1000$. Fig. 3 shows the relation curves between non-dim tensile force $F/(W\bar{\sigma}_{\mathrm{Y}})$ and elongation ratio U/L with 10×25 meshing for the three constitutive theories. It can be obviously observed that except J2F theory, clear shear bands are found from the simulated results of QFC and J2D theories whichever meshing divisions, and in the post-bifurcation simulation, the non-dim tensile forces obtained by the three kinds of theories show their explicit difference. A remarkable fact is that the localization calculated with J2F theory is much later than that with J2D theory and the localizations calculated with QFC theory are located between them. Moreover, a severe shear band is shown in the last one of Fig. 2(a) and (b), and no shear band forms in the second one of Fig. 2(a) and (b) for J2F theory. But, the shear band for QFC theory is moderate. If one notes the evolving processes of the quasi-elastic modulus E_{Q} in Eq. (2) during plastic deformation and compares with other two theories else, it can be understood that the above simulated results of the QFC theory are reasonable. For a small m value, numerical results in Figs. 2 and 3 are presented that illustrate the localization behavior of slightly rate-dependent solids under static loading condition. If the m value is very small, one can consider that the effect of strain rate dependence is very little, so as to be neglected. So, three kinds of

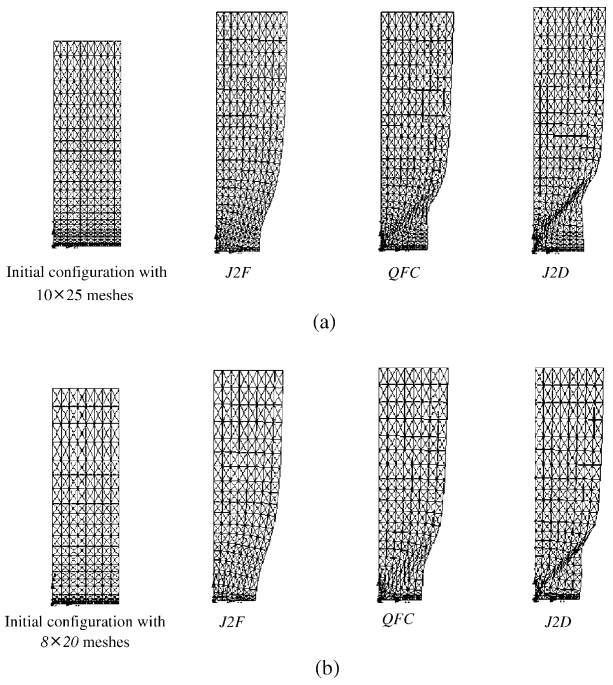

Fig. 2. Localization necking and shear bands obtained by three theories with $m = 0.001$ and $v_F = 1000$. (a) Final configurations simulated with 10×25 meshes, (b) final configurations simulated with 8×20 meshes.

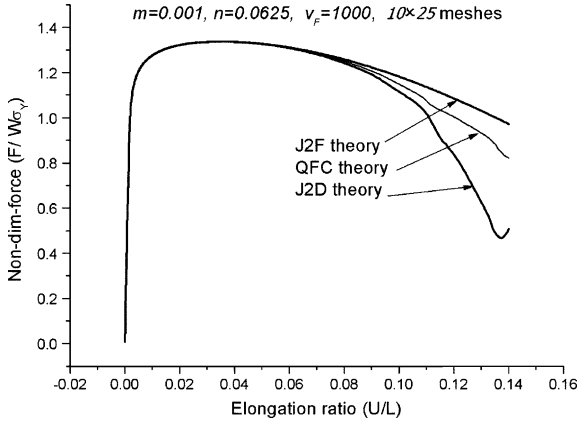

Fig. 3. Relationship between non-dim tensile force and elongation ratio for three constitutive theories.

theories will come back to their original forms with no rate-dependence. At this rate, the QFC theory with rate-independence and with slightly rate-dependent solids should get more reasonable results compared with those of J2F and J2D theories, from the viewpoint that normality rule of plastic flow gradually evolves into non-normality rule with vertex effect due to the basic ideal that the vertex effect of ''yield surface'' gradually appear throughout the whole plastic deformation processes from initial yielding to bifurcation and post-bifurcation up to final localization fracture discussed by Hu et al. (1998a,b).

The following discusses involve material rate dependence and mesh sensitivity of three constitutive theories in localization problems. In effect, material rate dependence implicitly introduces a length scale into the governing equation, although the constitutive description does not contain a parameter with the dimensions of length studied by Needleman (1988). The present simulation results obtained by different constitutive theories further certify the basic characteristic, and discover some new characteristics. Fig. 4(a)–(c) shows the effects of the two different meshing sizes and three different rate sensitivity exponents on the non-dim tensile force $F/(W\bar{\sigma}_Y)$. It can be obviously seen that the meshing sizes obviously affect the post-bifurcation behaviors of the non-dim tensile force no matter which constitutive theory, when the rate sensitivity exponent m is taken to be a relative small value. As the m value increases, the pathological mesh size effects associated with numerical solutions of post-bifurcation problem gradually disappear, especially for an obviously large m value ($m = 0.02$), the simulated results from three theories are almost superposed. Fig. 5(a) and (b) show the final configurations with 10×25 mesh size simulated from the three m values and by J2D and QFC theories, respectively. The configurations further illustrate that whether the J2D theory or QFC theory is used, the shear band gradually broadens so much as clears away, as the rate sensitivity exponent m increases. When the m value increase to a extent, such as 0.02, the appearances of the final

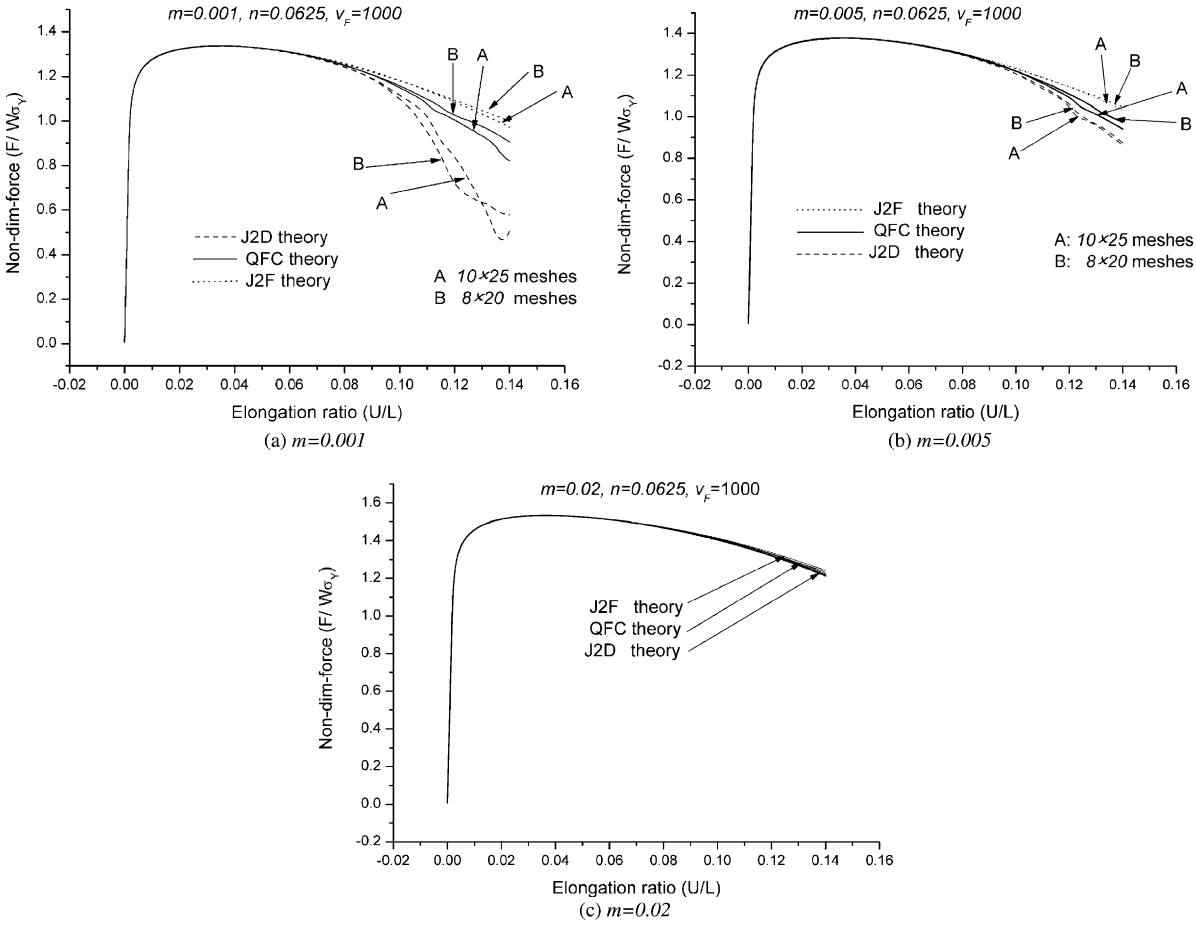

Fig. 4. Relationship between non-dim tensile force and elongation ratio with two kinds of meshing sizes and different m values simulated by three theories.

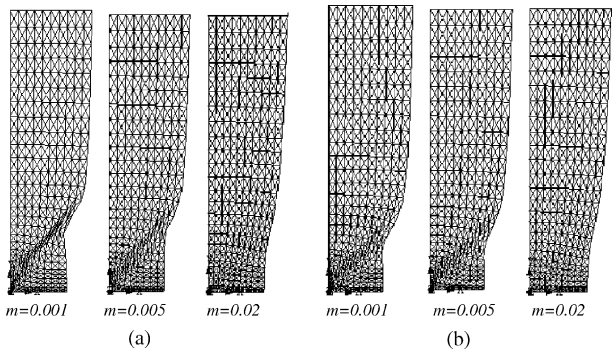

Fig. 5. (a) Final configuration obtained by J2D theory and with different m values. (b) Final configuration obtained by QFC theory and with different m values.

configurations from J2D and QFC theories are almost the same with that from J2F theory shown in Fig. 2(a). This phenomenon makes us know that the plastic constitutive theories with rate dependence can efficiently restrain the pathological mesh size effects, weaken the strain localization behavior involving shear band deformation and lengthen plastic deformation ability of materials during the post-bifurcation process. It can also be concluded that the difference of all of the numerical results in the present paper induced by different plastic constitutive theories, such as J2F, J2D, QFC and others else introduced in the past paper of Hu et al. (1998a,b), will be reduced. In general, the strain rate sensitivity of metal materials is not so much large, within about 0.0005–0.01, so the simulated results from different constitutive theories with rate dependence should be different, and the QFC theory should obtain more reasonable results compared with the other two theories, from the above discusses.

Finally, using the QFC theory, effects of the rate sensitivity exponent m and the non-dim tensile speed v_F on non-dim tensile force and necking ratio along the cross-section of the specimen's center shown in the first one of Fig. 2(a) and (b) are simulated. Figs. 6 and 7 show the effects of the m and v_F values on non-dim tensile force and necking ratio with 10×25 meshing, respectively. It can be found from Fig. 6 that when a constant v_F value is taken in advance, the larger the m value is taken, the larger the non-dim tensile force is needed, and the smaller the necking ratio on the condition of the same elongation ratio. On the other hand,

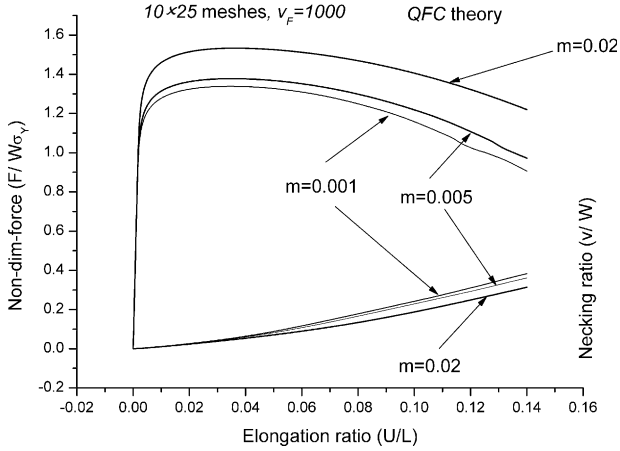

Fig. 6. Effects of different m values on non-dim tensile force and necking ratio obtained by QFC theory and with 10×25 meshes.

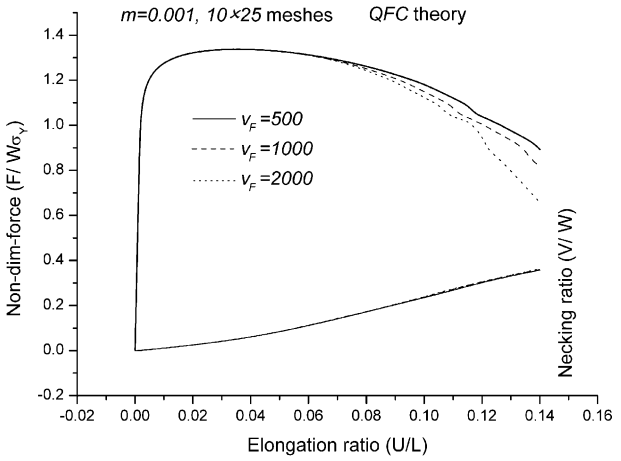

Fig. 7. Effects of non-dim tensile speeds on non-dim tensile force and necking ratio obtained by QFC theory and with 10×25 meshes.

it can be also noted from Fig. 7 that if taking a constant m value (0.001), although the non-dim tensile force shows obvious difference during post-bifurcation stage due to different v_{F} values, the v_{F} values have almost no effects on the necking ratio.

4.2. Sheet metal forming

A lot of experiments have shown that steels display positive strain rate dependence, which can be found from Simunovic and Shaw (2000) and Engl and Drewes (2000), and in general, higher punch speed results in higher strain rate. As a result, steels have higher strengths and consequently higher energy absorption. Preliminary studies confirmed that utilization of the phenomenon could assist in lightweighting.

Fig. 8 shows typical changes of true stress–true strain curves with different tensional strain rates for a TRIP 450/800 steel sheet under uniaxial stretching, from which it can be found that the stress values on the true stress–true strain curves orderly increase as the tensional strain rate does.

In order to recur the phenomenon by numerical simulation scheme and to verify the validity of the proposed rate-dependent quasi-flow corner plastic theory with punch speed sensitivity, another uniaxial stretching testing of the HPC35 high tensional steel sheet is simulated by Penazzi et al. (1992), which is with differential crosshead tensile speeds and convenient for comparing between theoretical model and experimental method. The initial configuration, size and finite element meshing of the specimen are shown in Fig. 9, in which sheet thickness is 0.66 mm, meshed element number 2312 and nodal number 2466. Material parameters are given in Penazzi's test (1992) and calculated in terms of the initial material parameters, which are shown as follows:

$$n = 0.25, \quad m = 0.007, \quad \dot{\bar{\varepsilon}}_{\mathrm{p}}^{0} = 10^{-3}\ 1/\mathrm{s}, \quad A = 623\ \mathrm{MPa}, \quad \bar{\varepsilon}_{\mathrm{p}}^{0} = 0.0,$$

$$E = 65875\ \mathrm{MPa}, \quad \mu = 0.3, \quad \text{yield strain } \bar{\varepsilon}_{\mathrm{Y}} = 0.002, \quad \text{yield stress } \bar{\sigma}_{\mathrm{Y}} = 131.75\ \mathrm{MPa}$$

The material is assumed to be isotropic and obey *Mises* yield criterion. Before stretching, the AB end of the specimen is fixed, and then the another end CD is drawn with three differential crosshead speeds, $\dot{u} = 5$, 500 and 6000 mm/min. The same problem is simulated by introducing the three kinds of speed values into the above finite element formulation. During calculation of the element matrices of the RDKQM, six-point

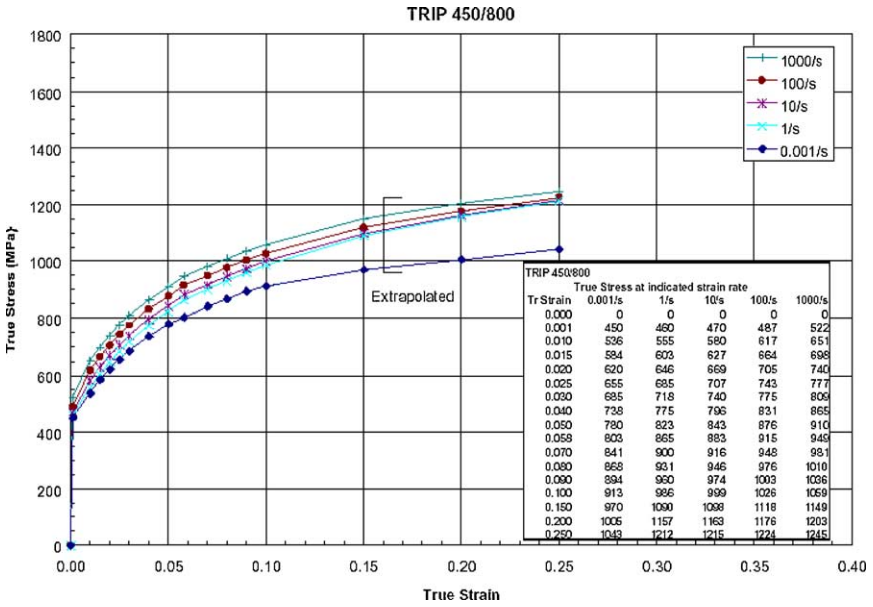

Fig. 8. True stress–strain curves with different tensional strain rates for a TRIP 450/800 steel sheet under uniaxial stretching.

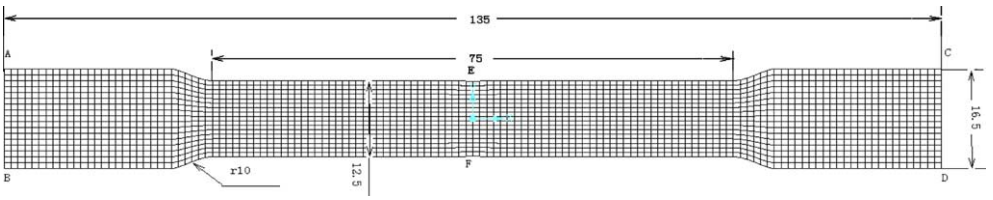

Fig. 9. Initial configuration, size and finite element meshing of the uniaxial stretching specimen. Sheet thickness: 0.66 mm; element number: 2312; nodal number: 2466.

Lobatto integration, four-point *Gauss* integration and one-point integration are used in the thickness direction, bending stiffness and shearing stiffness, respectively.

Fig. 10(a) and (b) shows the tensile force curves of the CD end versus the crosshead displacement and the true stress–plastic strain curves of the EF section, respectively. It can be clear found from Fig. 10(a) that different drawing rates result in obvious changes of not only the height and maximum value of the tensile force curves, but also the instability and necking points of the drawn specimens. As the crosshead speed increases, the critical tensile lengths when the specimens begin necking gradually decrease (seen in Table 1).

The phenomenon obtained by numerical simulation is in consistent with most experimental ones, it is to say, the necking and deformation localization of the specimens are brought forward as the crosshead drawing speed increases. Comparing with given experimental results, the present theoretical model and FEM are in very agreement with the measured values, the maximal error being 4.09%, which shows the validity of the present theoretical model.

Fig. 10(b) shows the true stress–plastic strain curves on the section EF ($x = 0$ section) of the specimen, from which very good agreement between experimental results and numerical simulation ones can be found in the scope of measured data points, the maximal error being 4.2%.

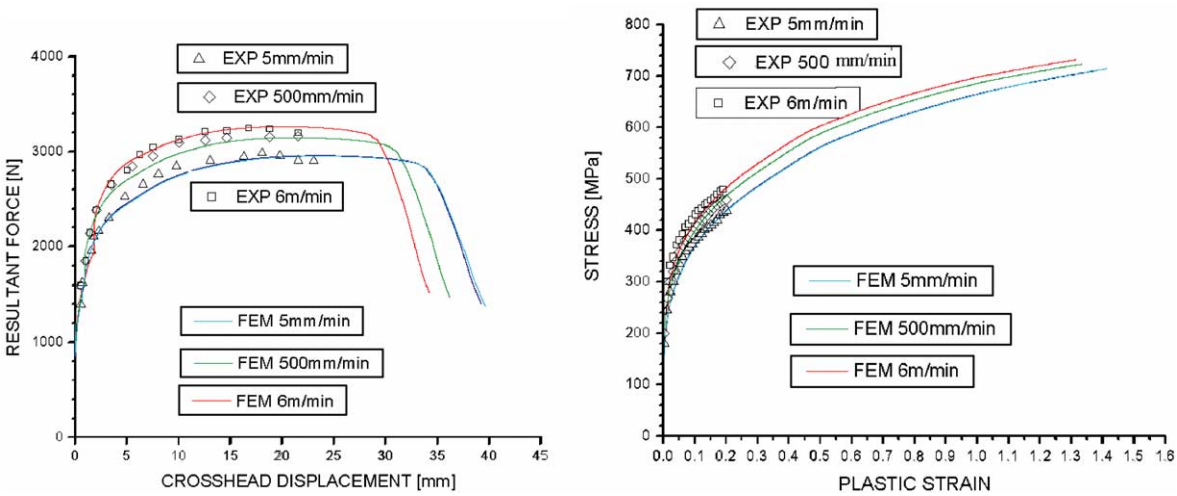

Fig. 10. (a) Tensile curves of the tensile force with crosshead displacement on the CD end. (b) True stress–plastic strain curves of the EF section.

Table 1
Critical tensile lengths with different crosshead speeds when specimens begin necking

Crosshead speed (mm/min)	Critical tensile length when specimen begins necking (mm)
5	23.7446
500	21.2803
6000	20.2867

Another numerical test is the square cup drawing with a circular blank. The commonly used 08Al steel sheet with a sheet thickness of 0.8 mm is taken as testing and simulated specimens. From uniaxial tests, some material constants were determined and shown as follows:

$$n = 0.248, \quad m = 0.01, \quad \bar{\varepsilon}_{\mathrm{p}}^{0} = 0.0, \quad \dot{\bar{\varepsilon}}_{\mathrm{p}}^{0} = 10^{-3}\ 1/\mathrm{s}, \quad A = 540\ \mathrm{MPa},$$

$$E = 207\ \mathrm{GPa}, \quad \mu = 0.3, \quad \text{yield strain } \bar{\varepsilon}_{\mathrm{Y}} = 0.002, \quad \text{yield stress } \bar{\sigma}_{\mathrm{Y}} = 110.3\ \mathrm{MPa}.$$

A quarter of circular blank with radius 45 mm is used to simulate the square cup drawing process due to material and structural symmetry. Fig. 11(a) shows the geometry and dimensions of the punch and die, and finite element meshing of a quarter of circular sheet, in which element number and nodal number are 503 and 547 (seen in Fig. 11(b)), respectively. Three punch speeds, i.e., $\dot{u} = 50$, 100 and 150 mm/s, are set up in the present experiment and numerical simulation. During the stamping calculation, common contact algorithm proposed by Li et al. (2002) and *Coulomb* friction law are used, in which the friction coefficients of the contact surfaces of the stamped sheets corresponding to the punch, die and binder are taken to be 0.2, 0.1 and 0.1, respectively. Fig. 12(a) and (b) shows the experimental and the numerical simulated results (the quarter of circular blank) of the final deformation configuration with maximal drawing length 40 mm when punch speed is 100 mm/s. Two typical sections on the blank are taken as tested ones, one being the section AB along the diagonal direction and another being the section AC along the cross-section direction on the initial blank (seen in Fig. 11(b)). Fig. 13(a) and (b) shows the thickness distributions on the sections AB and AC with different punch velocities and corresponding to the final configuration. The actual thickness values

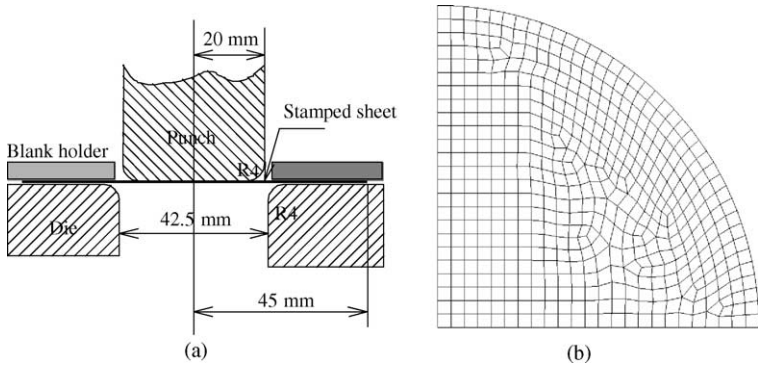

Fig. 11. Geometry and dimensions of the punch and die, and element meshing of one quarter of circular sheet: (a) square cup drawing test of circular sheet, (b) finite element meshing of 1/4 circular sheet.

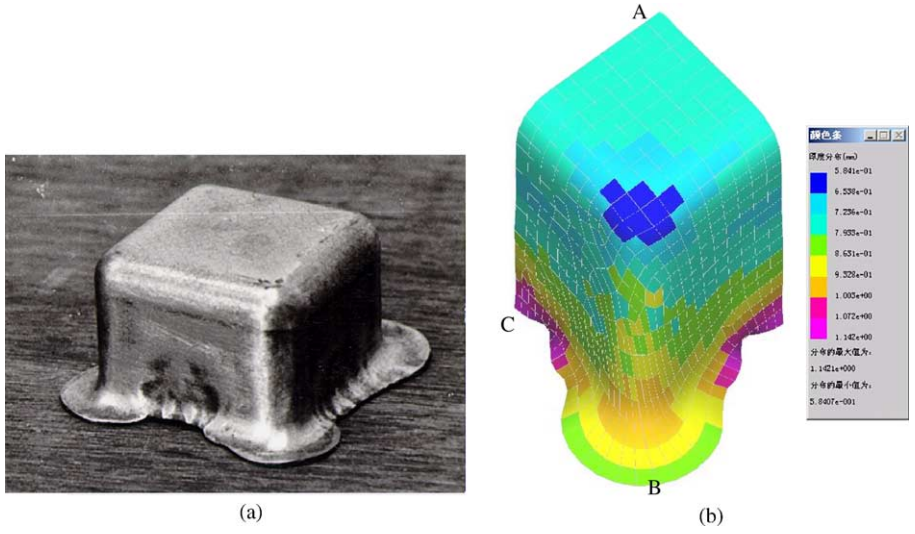

Fig. 12. (a) Final deformation configuration obtained by experiment with punch speed $\dot{u} = 100$ mm/s. (b) Final configuration and element meshing.

on the sections AB and AC in experiments are measured by a TM1-CD type thickness-detected instrument made by Stress Tel Company in America. It can be obviously found that there is in good agreement between experiments and simulated results. An evident fact is that the loading conditions with faster punch machine velocity result in faster thinning within the region where blank is markedly stretched.

In order to show the ability of the present strain rate dependent plasticity model to deal with localized thinning and strain localization during deep-drawing processes, for a given punch speed $\dot{u} = 100$ mm/s, the effects of strain rate sensitivity on the thickness distribution of the sections AB and AC are further studied by taking the stain rate sensitivity exponent m in Eq. (28) to be 0.001, 0.01 and 0.1, respectively. Fig. 14(a) and (b) shows thickness thinning characteristics on the sections AB and AC. It can be found from Fig. 8 that the strain rate dependent plasticity model with larger m value restrains the localizing thinning and makes the thickness distribution trend to more smooth and more uniform; On the other hand, when the m

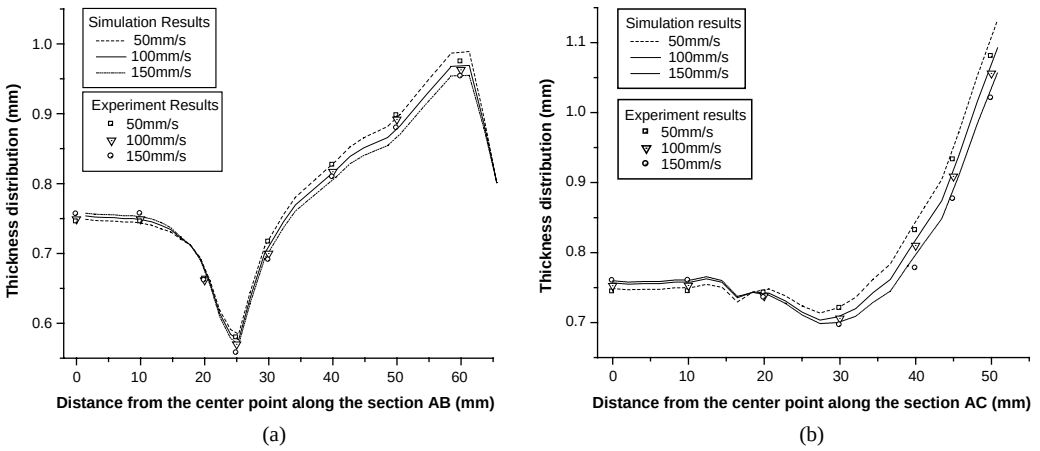

Fig. 13. Final simulation results for the thickness distribution: (a) along AB section, (b) along AC section.

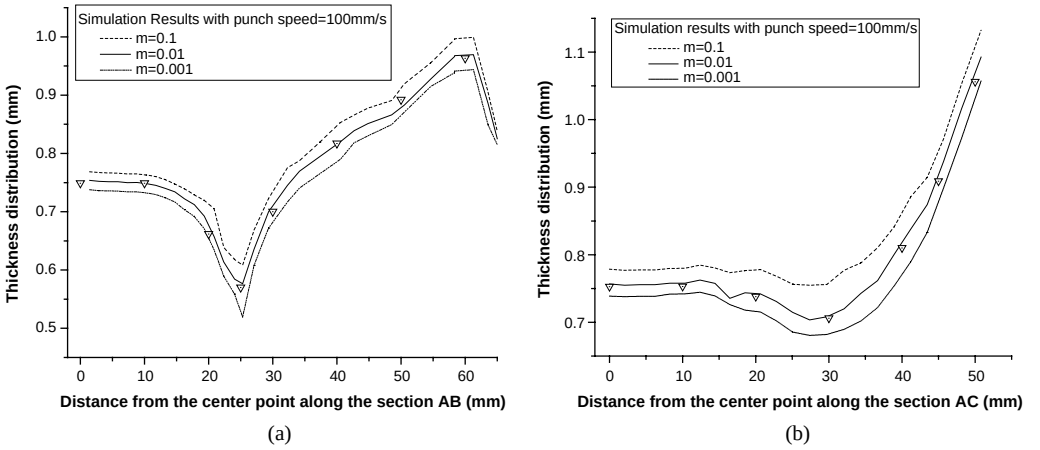

Fig. 14. Effects of the strain rate sensitivity exponent m on thickness distributions: (a) along AB section, (b) along AC section.

value is taken to be 0.001, a very small value, the effect of the strain rate sensitivity becomes not half, and a rapid localizing thinning appears on the corner of specimen.

The final numerical example is an industrial forming test, in which an oil pan made in the First Automobile Manufacture in China is stamped by a hydraulic pressure machine with different punch speeds. The die structure of the oil pan is modeled by the famous CAD software CATIA, including punch, blankholder and die-face model, which is shown in Fig. 15. In the forming test, maximal drawing depth, closing punch and die, is 208 mm. The punch speed is previously adjusted as $\dot{u} = 100$ mm/s. The formed sheet metal is a 08ZF material and its initial thickness $h_0 = 1.5$ mm. the friction coefficients of the contact surfaces of the stamped sheets corresponding to the punch, die and binder are taken to be 0.15, 0.15 and 0.1, respectively. Material parameters are given as follows:

$$n = 0.24, \quad m = 0.01, \quad \bar{\varepsilon}_{\mathrm{p}}^{0} = 0.0, \quad \dot{\bar{\varepsilon}}_{\mathrm{p}}^{0} = 10^{-3}\ 1/\mathrm{s}, \quad A = 540\ \mathrm{MPa},$$

$$E = 200\ \mathrm{GPa}, \quad \mu = 0.25, \quad \text{yield strain } \bar{\varepsilon}_{\mathrm{Y}} = 0.002, \quad \text{yield stress } \bar{\sigma}_{\mathrm{Y}} = 112\ \mathrm{MPa}.$$

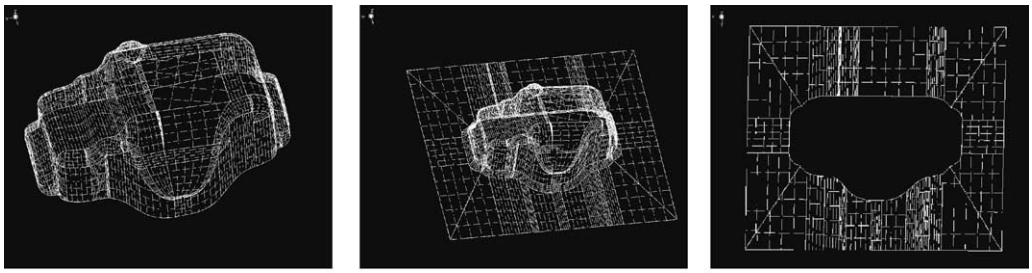

Fig. 15. The die structures of the oil pan: (a) punch surface, (b) die surface, (c) blankholder.

The shape of the blank sheet and finite element meshes discredited into 6976 RDKQM elements are shown in Fig. 16. Two important relation lines involving with the influence of punch speed are shown in Figs. 17 and 18. The former gives the comparison trending lines of maximal drawing depth with different punch speeds, which are obtained by the present FEM and by experimental results measured using the TM1-CD type thickness-detected instrument, when the thickness value h_{A_1} on the dropping oil hole (seen in Fig. 19); and the latter is another relation lines between the thickness value h_{A_1} and punch speed, when the drawing depth reaches 188 mm. It can be remarkably found from the two figures that the maximal drawing depth value decreases as punch speed increases if a fixed thickness value on dropping oil hole is taken to be critical criterion; on the other hand, the thinning of the thickness h_{A_1} on the dropping oil hole increases as punch speed does if the drawing depth reaches a fixed value. The evolutive trends are qualitatively coincident with that measured from experiments.

In order to further investigate the validity of strain rate sensitivity model, the rate sensitivity exponent m is again taken to be 0.001, 0.01 and 0.1, respectively; and three special measuring points A_1, A_2, and A_3 shown in Fig. 19 are used to check the simulated accuracy of the present QFC theory. Table 2 gives a detail comparison. It is obviously seen that the present model gets very agreement results compared with experimentally measured thickness values on the special points, especially when the m value is taken to be 0.01.

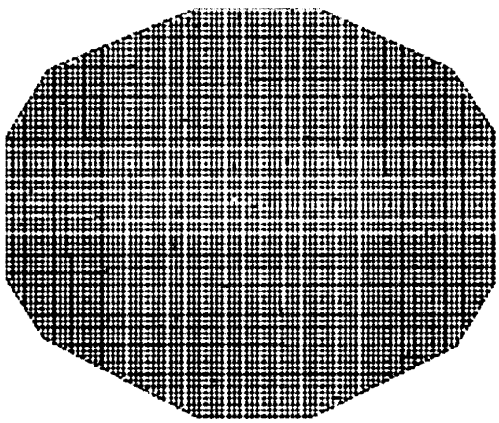

Fig. 16. Shape of blank sheet and its FEM meshing.

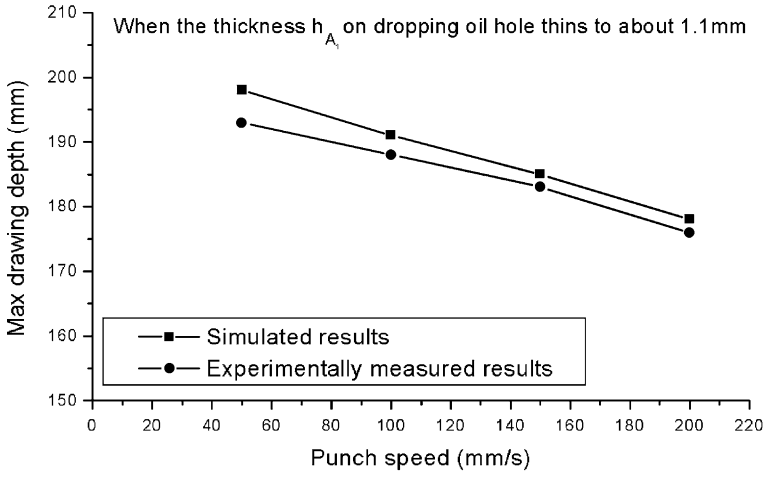

Fig. 17. Maximal drawing depth with different punch speeds ($m = 0.01$).

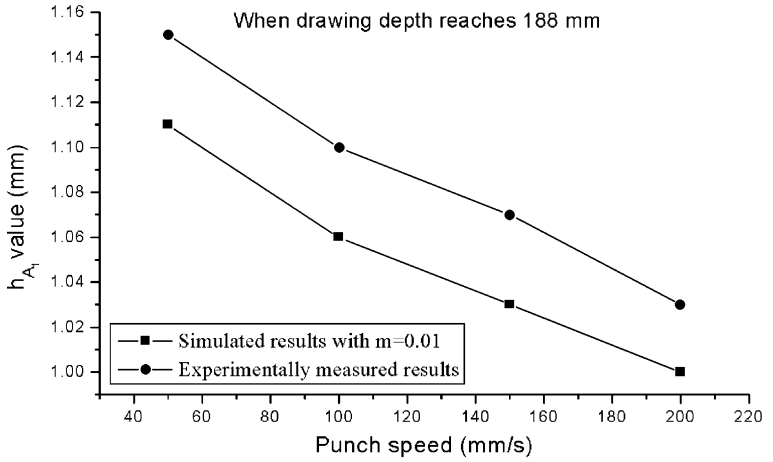

Fig. 18. The thickness values on the dropping oil hole A_1 with different punch speeds.

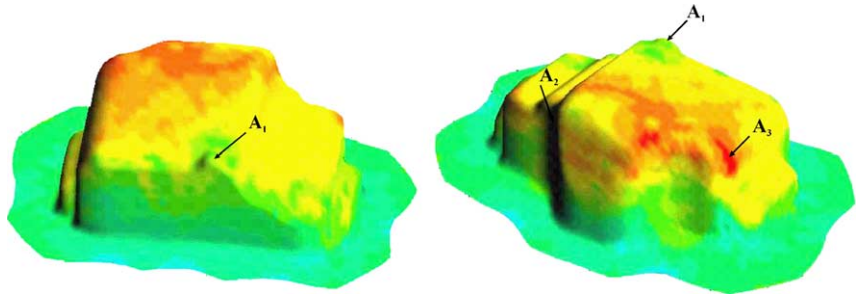

Fig. 19. Thickness distribution of the final configuration simulated by QFC theory with the punch speed $\dot{u} = 100$ mm/s.

Table 2
Comparison within experimentally measured results and the present model when the punch moves to maximal drawing depth 208 mm

			h_{A_1} (mm)	h_{A_2} (mm)	h_{A_3} (mm)
Present model	$\dot{u} = 100$ mm/s	$m = 0.001$	0.88	1.03	1.12
		$m = 0.01$	0.99	1.08	1.19
		$m = 0.1$	1.05	1.16	1.28
Experimentally measured values $\dot{u} = 100$ mm/s			1.01	1.11	1.20

5. Conclusions

Many metal materials represent their strain-rate dependency. Especially when materials go through large plastic deformation, the strain-rate dependency appears more obvious. Different speed boundary conditions, such as crosshead speed and punch speed, result in the change of strain-rate of materials, which can be introduced into the plasticity constitutive model by so-called *Hollomon* formula. In the present paper, the strain-rate dependent quasi-flow corner plastic constitutive theory is proposed for elastic visco-plasticity materials with large-deformation, and punch speed sensitivity is introduced as the special speed boundary condition in terms of the above consideration. Two classical rate-dependent isotropic plasticity theories, the J2F and J2D theories, are compared with the present theory for plane strain tensile test. It has been found from a lot of numerical examples that the rate-dependent plastic constitutive theories can efficiently restrain the pathological mesh size effects, weaken the strain localization behavior involving shear band deformation and lengthen plastic deformation ability of the elastic/visco-plastic materials. It can also be concluded that the difference of all of the numerical results in the present paper induced by different plastic constitutive theories, such as J2F, J2D, QFC and others else introduced in the past paper (Hu et al., 1998a,b), will be reduced. In general, the strain rate sensitivity of metal materials is not so much large, so the simulated results from different constitutive theories with rate dependence should be different, and the QFC theory should obtain more reasonable results compared with the other two theories. The uniaxial tensile test, the deep-drawing test of circular blank with square punch and the actual industrial stamping test of an oil pan deep-drawing further show that numerical simulation results obtained by QFC theory are in good agreement with experimental ones, which exhibit the validity of the present theory and calculation model.

Acknowledgements

This work was all together supported by the Scientific Foundation of National Outstanding Youth of China (no. 10125208), the Key Project of National Natural Science Foundation of China (no. 19832020), and the Key Project of the National Education Committee of China. The author thanks his students, Dr. Haipeng Liu, for providing simulating data and making significant discussions.

References

Budiansky, B., 1959. A reassessment of deformation theories of plasticity. Trans. ASME, J. Appl. Mech. 1, 259.

Chandra, A., 1986. A generalized finite element analysis of sheet metal forming with an elastic–viscoplastic material model. Trans. ASME, J. Eng. Ind. 108, 9.

Chen, W.J., Cheung, Y.K., 2000. Refine quadrilateral element based on Mindlin/Reissner plate theory. Int. J. Numer. Meth. Eng. 47, 605.

Christofferson, J., Hutchinson, J.W., 1979. A class of phenomenological corner theories of plasticity. J. Mech. Phys. Solids 27, 465.

Engl, B., Drewes, E.J., 2000. New high strength steels with good formability for automotive applications. In: ATS Conf., Paris, December.

Germain, Y., Chung, K., Wagner, R.H., 1989. A rigid-visco-plastic finite element program for sheet metal forming analysis. Int. J. Mech. Sci. 31, 1.

Gotoh, M., 1985. A class of plastic constitutive equations with vertex effect—I. General theory. Int. J. Solids Struct. 21 (11), 101.

Hart, E.W., 1976. Constitutive relations for the nonelastic deformation of metals. Trans. ASME, J. Eng. Mater. Technol. 193, 22.

Hu, P., Lian, J., Liu, Y.Q., Li, Y.X., 1998a. A quasi-flow corner theory of elastic plastic finite deformation. Int. J. Solids Struct. 35 (15), 1827.

Hu, P., Na, J.X., Li, D.Y., 1998b. Bifurcation and post bifurcation behavior in sheet metal tension with strong anisotropy. J. Mater. Proc. Technol. 74, 276.

Hu, P., Liu, Y.Q., Wang, J.C., 2001. Numerical study of the flange earring of deep-drawing sheets with stronger anisotropy. Int. J. Mech. Sci. 43, 279.

Huang, Y.H., Liu, C.H., 1994. The effects of strain rate and anisotropy upon the sheet-stretching process. Int. J. Mech. Sci. 36 (4), 105.

Hutchinson, J.W., 1974. Plasticity buckling. Adv. Appl. Mech. 14, 67.

Kim, J.H., Oh, S.I., Kobayashi, S., 1978. Analysis of stretching of sheet metals with hemispherical punch. Int. J. Mach. Tool Des. 18, 209.

Li, D.Y., Hu, P., Cao, Y., Wang, J.C., 2002. Section analysis of industrial sheet-metal stamping processes. J. Mater. Proc. Technol. 120, 37.

McMeeking, R.M., Rice, J.R., 1975. Finite element formulation for problems of large elastic–plastic deformation. Int. J. Solids Struct. 11, 601.

Nagtegaal, J.C., Parks, D.M., Rice, J.R., 1974. On numerically accurate finite element solution in the fully plastic range. Comp. Meth. Appl. Mech. Eng. 4, 153.

Nagtegaal, J.C., Jong, J.E.De., 1981. Int. J. Numer. Meth. Eng. 17, 51.

Neale, K.W., 1981. Phenomenological constitutive laws in finite plasticity. SM Arch. 6 (1), 79.

Needleman, A., 1988. Material rate dependence and mesh sensitivity in localization problems. Comp. Meth. Appl. Mech. Eng. 67 (1), 69.

Park, J.J., Oh, S.I., Altan, T., 1987. Analysis of axisymmetric sheet forming processes by rigid-viscoplastic finite element method. Trans. ASME, J. Eng. Ind. 109, 347.

Penazzi, L., Pasquale, E.Di., Aita, S., Haug, E., Levaillant, C., Priadi, D., 1992. Material characterization for the CAE finite element simulation of sheet material forming. In: Proc. 17th IDDRG Congr., Shenyang, China, p. 149.

Simunovic, S., Shaw, J., 2000. Effect of strain rate and material processing in full vehicle crash analysis, SAE Technical Paper, No. 2000-01-2715. Society of Automotive Engineers, Warrendale, PA, USA.

Storen, S., Rice, J.R., 1975. Localized necking in the sheet. J. Mech. Phys. Solids 23, 421.